ORIGINAL RESEARCH

The Institution of Engineering and Technology | WILEY

Performance analysis of ground-based long baseline radar distributed systems for space situational awareness

Sebastián Díaz Riofrío[1] | **Simão Da Graça Marto**[2] | **Christos Ilioudis**[1] |
Massimiliano Vasile[2] | **Carmine Clemente**[1]

[1]Electronic and Electrical Engineering, University of Strathclyde, Glasgow, UK

[2]Mechanical and Aerospace Engineering, University of Strathclyde, Glasgow, UK

Correspondence

Sebastián Díaz Riofrío.
Email: sebastian.diaz-riofrio@strath.ac.uk

Abstract

Detection of space objects is a key component of space situational awareness, which could help prevent and minimise space collisions. While there have been lots of radar systems designed to detect space objects, few of them have dealt with long baseline distributed bistatic pairs. The authors focus on the feasibility of long baseline bistatic radars, which can be extended for the multistatic case; and the performance of the multistatic system for a target at different altitudes assuming one transmitter over three different scenarios: a cluster of receivers, receivers spread throughout the world and the combination of the two previous cases. To analyse the performance the multiple-input-multiple-output (MIMO) ambiguity function (AF) will be employed. The results of the MIMO AF show how the fusion of different bistatic pairs improves the detection capabilities. Moreover, when the different radar measurements are coherently summed in the MIMO AF, the uncertainty on the location of the target is reduced.

KEYWORDS

MIMO radar, radar, radar signal processing, space debris

1 | INTRODUCTION

In recent years the amount of space objects orbiting around the Earth has increased dramatically, which has led to a higher chance of collision. According to the 2021 space environment report from the European Space Agency (ESA) [1], the number of objects larger than 10 cm in low Earth orbit (LEO) is over 36,500, and the number objects larger than 1 cm is over a million. Moreover, as launching micro-satellites for commercial and scientific purposes has become more affordable, the LEO space is getting crowded. Therefore, the detection of space objects has become an important topic to research.

Radar has been widely used for space situational awareness (SSA) to detect and track cooperative objects orbiting around the Earth, such as satellites, or uncooperative objects, such as space debris. While there has been an encouragement to develop space-based SSA radar [2, 3], most of the radar SSA systems are Earth-based. Most SSA radar work in a monostatic configuration, where the transmitter and receiver are in the same position. Nonetheless, there are some that work in a bistatic arrangement [4], where the transmitter and receiver are in different locations. Many of the SSA systems use radio telescopes, mainly as receivers as they have better sensitivity, improving the detection of targets with smaller radar cross section (RCS), and possibly smaller targets, for a given range [5, 6]. However, the bistatic angle is not large enough so that the bistatic advantages can be exploited and most of these systems work in a quasi-monostatic configuration [7].

When multiple transmitter–receiver bistatic pairs are combined, multistatic systems are created. Regarding the role of multistatic systems in SSA, there have been some studies on multistatic radars [8, 9] for detecting space objects, but a limited number of them used long baseline bistatic pairs. In this paper, by *long baseline* it is understood a distance from transmitter to receiver of 5000 km, or greater. Additionally, a bistatic radar would be considered any radar system that results in a bistatic angle, β, greater than 10° [8, 9], where systems with these characteristics were considered bistatic. In ref. [8], as part

of the German Experimental Surveillance and Tracking Radar (GESTRA), transmitter and receiver units were built and assessed to create a multistatic system with a maximum baseline of 500 km to detect a target at an altitude of 1000 km. The configuration resulted in a bistatic angle of 14°. In ref. [9] using a baseline of 250 km was employed to create a bistatic system to perform SAR imaging on a target at 627 km. This system utilised a bistatic angle of 11°. A more recent experiment was conducted on [10], where a transmitter in Millstone Hill, USA, was used along with two receivers, placed in Westerbork, Netherlands, and Sardinia, Italy, which created a bistatic angle of around 8° and 10°, respectively, with baselines of 5650 and 5500 km, respectively. Although, for now, the multistatic performance of the system has not been shown.

A longer baseline will enable the system to better exploit the bistatic capabilities in a multistatic configuration and reduce the ambiguity in the target location derived from the radar measurements. Configuring the multistatic system to work in a bistatic way, instead of a monostatic or quasi-monostatic configuration, will allow distributing sensing and to capture different target returns from the same transmission. Hence, if one of the bistatic pairs returns in an incorrect location detection of the target because of its low signal-to-noise ratio (SNR), the other readings could help to detect it correctly, as seen in Section 4. Moreover, multi-static radars can offer better behaviour characterisation of the space object [11]. Being able to have multiple receivers in the multistatic radar will open the possibility of increasing the SNR of the target if the fusion of the radar data is performed with proper methods, such as the multiple-input-multiple-output (MIMO) ambiguity function (AF).

The paper will examine the feasibility of long-based radars along with the advantages in the performance and detection capability of multistatic radar systems. One key issue, not thoroughly discussed in the paper, is the synchronisation problems that might arise from having receivers and transmitters in different continents. Nonetheless, several solutions have been proposed to synchronise digital systems, principally using GNSS signals [12, 13].

In Section 2, the characterisation of the bistatic pairs and overall multistatic system will be laid out with some of the challenges regarding the use of radar in SSA. Section 3 will show the results of the conducted feasibility study for one bistatic pair, as the rest of them will be similar. The performance of the multistatic system with different configurations will be presented in Section 4, where the MIMO AF, introduced in Section 2.3, is going to be used to analyse the system. Finally, the conclusions of the study and possible future work will be explained in Section 5.

2 | RADAR SYSTEM CHARACTERISATION

For the system characterisation various components and properties of the employed radar system are introduced. These are going to be used in later simulations and analysis. At the current stage the system would only be able to detect small satellites in LEO, around half the size of a Starlink satellite, and large satellites in GEO, as discussed in Section 3.2.

The radar system will not be a search radar, and, as such, it will not be scanning the whole space, from horizon to horizon. Since many space objects, from satellites to space debris, have two-line element (TLE) sets [14], the ephemerides, the trajectories, of these could be calculated. The position of said space objects could be estimated and, using this prior knowledge, the radio telescopes could be pointed to that location. Once this is completed, the signal processing, using the MIMO AF, could be performed and a constant false alarm rate (CFAR) detector [15] could be used to detect the possible targets.

2.1 | Bistatic radar

In a classical radar system, the transmitter and receiver are situated in the same locations and, many times, use the same antenna for transmission and reception purposes, forming what is called a monostatic configuration.

On the contrary, a bistatic radar would use a transmitter and a receiver in different locations. In SSA, due to their high sensitivity, radio telescopes are often used as receivers in conjunction with radar transmitters to form bistatic pairs. Nevertheless, due to the relatively small distance between the transmitter and receiver compared to the target location, most bistatic SSA systems do not form large enough bistatic angles and can be considered quasi-monostatic.

Indeed, a key property of a bistatic radar is its bistatic angle, β, which is the angle with vertex at the location of the target and rays at the transmitter-target and target-receiver paths. Figure 1 shows the basic bistatic configuration. The transmitter, Tx, and receiver, Rx, are separated by a distance, $L_{Tx,Rx}$, also called the baseline, the target travels at a speed, v, while the distance from the transmitter to the target is denoted by d_{Tx} and the distance from the receiver to the target by d_{Rx}. A system can be considered bistatic if $\beta > 0$. There is an exception though if $\beta \simeq 0$ while $L_{Tx,Rx} \neq 0$, then the system is considered quasi-monostatic. For example, in ref. [4] a bistatic system was used to detect a satellite at 800 km with a baseline of about 10 km. The estimated bistatic angle of this
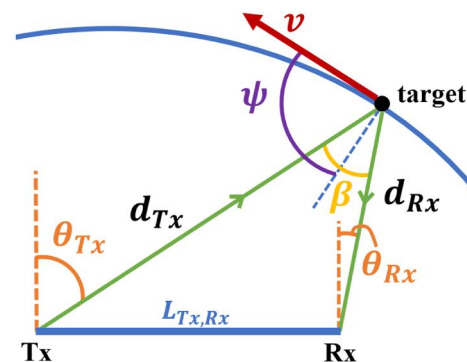

FIGURE 1 Bistatic configuration.

configuration was 0.72°, an angle associated with quasi-monostatic configurations.

When considering earth-to-space observations, for a big enough bistatic angle to be achieved, which according to refs. [8, 9] should be around 10°; the transmitter and receiver will have to be separated by hundreds or thousands of kilometres, depending on the intended maximum altitude to be observed. For example, assuming a bistatic angle of 10° and $d_{Tx} \approx d_{Rx}$, if the target is at an altitude of 1000 km, a LEO satellite, the transmitter and receiver should be separated by 175 km, which is the distance between Nottingham and London. On the other hand, if the observed object is orbiting at 35,786 km, a geo-stationary (GEO) satellite, the minimum distance between transmitter and receiver for the radar system to be considered bistatic should be 62,617 km, the distance between Amsterdam and Washington DC. An example of a radar for SSA with a big bistatic angle was shown in ref. [16]. For the study, a system with a baseline of 916 km was used to detect a target at 620 km, which created an estimated bistatic angle of 72°.

One of the key features of the bistatic radar is the bistatic angle, β. The bistatic angle affects the bistatic RCS, $\mathrm{RCS_{bs}}$, of the target. Here the bistatic RCS will be modelled as follows [17]:

$$\mathrm{RCS_{bs}} \simeq \mathrm{RCS}\ \cos\frac{\beta}{2} \tag{1}$$

where RCS is the monostatic RCS and β is the bistatic angle.

The bistatic Doppler frequency is given by the following [18]:

$$f_D = \frac{2v}{\lambda} \cos\psi \cos\frac{\beta}{2} \tag{2}$$

2.2 | Multistatic radar

When the bistatic configuration is extended to multiple transmitters and/or receivers to form multiple bistatic pairs, a multistatic radar configuration is generated. The advantages of a multistatic radar lay on, not only the ability to increase the SNR, but also the capability of the radar to observe the target from different angles, which might increase the reflected RCS and decrease the ambiguity in the measurement.

The radar-range-equation (RRE) presented in ref. [7], can be extended for the multistatic case as follows:

$$\mathrm{SNR_{ms}} = \sum_{i}^{N} \sum_{j}^{M} \mathrm{SNR_{bs;}}_{i,j} \tag{3}$$

for the coherent fusion of the bistatic pair measurements, and as follows:

$$\mathrm{SNR_{ms}} \approx \sqrt{\sum_{i}^{N} \sum_{j}^{M} \mathrm{SNR_{bs;}}_{i,j}^{2}} \tag{4}$$

for the non-coherent fusion. Where, $\mathrm{SNR_{bs;}}_{i,j}$ is the SNR of the signal emitted from transmitter i and received in the j

receiver, and N and M are the number of transmitters and receivers.

2.3 | Multiple-input-multiple-output ambiguity function

A way to assess the performance and limits of a radar system is the ambiguity function (AF). The AF for a single transmitter and single receiver system is defined as the output of a matched filter for a certain waveform and different values of delay and Doppler shift [7]:

$$AF(\tau, f_D) = \int_{-\infty}^{\infty} s(t) \cdot s^*(t - \tau) e^{j2\pi f_D t} dt \tag{5}$$

with τ being the delay of the signal and f_D the Doppler shift.

The MIMO AF approach employed in this study was originally presented in ref. [19], naturally, it has been adapted for the case at hand. In a similar way as in ref. [20], the radar parameters of range and Doppler rate are replaced by its Cartesian equivalents of position and speed. The reason behind using Cartesian coordinates is that it will be more helpful for performing later SSA tasks [11] and is easier to visualise, having similar plots as in ref. [21]. In ref. [19] a AF is introduced for multiple-inputs-single-outputs (MISO) systems. If the MISO AF is generalised, the MIMO AF can be deduced. First, the AF of one of the bistatic pairs is described as follows:

$$AF_{i,j}(\vec{p}, \vec{v}) = \int_{-\infty}^{\infty} s_{i,j}(t, \vec{p}_k, \vec{v}_k) \cdot s_{i,j}^*(t, \vec{p}, \vec{v}) dt \tag{6}$$

where $\vec{p} = (x, y, z)$ is the position vector, $\vec{v} = (v_x, v_y, v_z)$ the speed vector, $s_{i,j}(t, \vec{p}_k, \vec{v}_k)$ is a signal transmitted from the transmitter i and received at the receiver j assuming a target at the position $\vec{p}_k = (x_k, y_k, z_k)$ with a speed of $\vec{v}_k = (v_{x,k}, v_{y,k}, v_{z,k})$. Note that compared to the traditional definition in Equation (5), here the delay and Doppler have been replaced with the 3-dimensional position and velocity parameters which allows us to use a common space for all sensor pairs.

Combining the AF of the different transmitter-receiver pairs, the MIMO AF can now be defined as follows:

$$AF(\vec{p}, \vec{v}) = \sum_{i=1}^{N} \sum_{j=1}^{M} AF_{i,j}(\vec{p}, \vec{v}) \tag{7}$$

Hence, here the MIMO AF is defined as the sum of the AF of the different bistatic pairs. In Equation (7), this sum is done coherently, also called coherent fusion, which implies that good synchronisation between the different sensors is necessary. An alternative approach is to sum the AF from the different pairs non-coherently, non-coherent fusion:

$$AF(\vec{p}, \vec{v}) = \sum_{i=1}^{N} \sum_{j=1}^{M} |AF_{i,j}(\vec{p}, \vec{v})| \qquad (8)$$

To reduce complexity, the AF in Equation (6) can be simplified if the different speed component values are replaced by the Doppler shift resulting from that speed:

$$AF_{i,j}(\vec{p}; f_{D;i,j}) = \int_{-\infty}^{\infty} s_{i,j}(t; \vec{p}, f_{D;i,j;k}) \cdot s_{i,j}^{*}(t; \vec{p} f_{D;i,j}) dt \qquad (9)$$

where $f_{D;i,j}$ is the Doppler frequency shift perceived from transmitter i at receiver j.

As different Doppler shifts are perceived from each bistatic pair, the $f_{D;i,j}$ returning the maximum response in each AF can be used to synthesise the MIMO AF:

$$AF(\vec{p}) = \sum_{i=1}^{N} \sum_{j=1}^{M} \max_{f_{D;i,j}} |AF_{i,j}(\vec{p}, f_{D;i,j})| \qquad (10)$$

$$AF(\vec{p}) = \sum_{i=1}^{N} \sum_{j=1}^{M} \max_{f_{D;i,j}} AF_{i,j}(\vec{p}, f_{D;i,j}) \qquad (11)$$

It should be noted in Equation (10) that the AF from the different pairs are added non-coherently. Furthermore, this definition can only be applied in the single target scenario or in the multiple target scenario with similar velocity parameters.

2.4 | Long baseline multistatic radar challenges in SSA

In SSA, the expected operating ranges are very large. This could result in aliasing problems in the Doppler processing specially when working with long baseline bistatic systems. For instance, assuming a transmitter in the Haystack Observatory, Massachusetts, USA, and a receiver near Westerbork, Netherlands, as in ref. [10], if the target to be detected is at an altitude of 600 km, the PRI should be at least 20.02 ms, an equivalent PRF of 49.96 Hz. This means that the maximum speed that the radar would be able to detect, assuming an operational frequency of 1.24 GHz is $v_{\max} = PRF \cdot \lambda/4 = 3.02$ ms^{-1}. The orbital escape speed is as follows [22]:

$$v_{esc} = \sqrt{\frac{2GM_{earth}}{r}} \qquad (12)$$

with G being the gravitational constant of the Earth, M_{earth} the mass of the Earth, and $r = R_{earth} + h_{tgr}$, R_{earth} being the radius of the Earth, and h_{tgr} the altitude of the satellite. Using Equation (12), the resulting speed of the target should be at least $v_{esc} = 10.69$ km s^{-1}. If the angular speed of the rotation of the Earth is considered, 72.92 μrad s^{-1}, the relative speed of the target is 10.19 km s^{-1}. By using Equation (2), with $\beta = 47.98°$, from the configuration in ref. [10] and $\psi = 80°$, so

that the Doppler is not zero, the perceived Doppler shift is $f_D = 13.73$ kHz. Thus, the PRF needed to detect the target would produce aliasing in Doppler. Consequently, a correct Doppler processing scheme must be adopted to avoid aliasing. In refs. [23, 24] solutions have been presented to solve the aliasing in space environments. Additionally, in ref. [25] a two-step solution is presented for high speed targets, and a similar approach could be taken to overcome the Doppler aliasing.

On the one hand, regarding coherent integration processing for LEO targets, as they have high speeds, the target would change between range bins and the coherent processing interval (CPI) would be small. Range compensation techniques would be needed to have larger CPIs. On the other hand, when it refers to the coherent fusion processing, by examining Equation (2) it is easy to see how different bistatic pairs will generate different Doppler shifts. To be able to implement coherent multiple fusion, Doppler compensation will be needed. The main implication for this issue is that between the bistatic pairs there must be good synchronisation and that the systems must be properly defined to account for phase errors or different Doppler frequencies.

In cases of GEO targets the relative speed is almost zero [26], as it matches the rotation of the Earth, so the multiple coherent integration, in this case, would be much more simple and less pre-processing for it will be necessary. The perceived zero-speed allows for longer integration times without range compensation, since the target does not change range bin. In addition, coherent multiple sensor fusion when using the MIMO AF is also more direct, as there is no need for Doppler compensation since the perceived speed is zero.

3 | RADAR SYSTEM VALIDATION

To validate the proposed radar system configuration, a series of simulations are going to be reproduced to assess the feasibility of the multistatic system. It must be mentioned that most of the results that are going to be shown are the outcomes of one of the bistatic pairs, since the rest of the results for the bistatic pairs are going to be similar. For the results to be as most realistic as possible, transmitter and receiver parameters of known radio telescopes are chosen.

3.1 | Transmitter and receiver

The transmitter used in the simulation is located in MIT Haystack Observatory, USA, and uses the Millstone Hill Radar (MHR). MHR is a 25.6 m radius full steerable mechanical antenna. The location of the receiver is in Cambridge, United Kingdom, and uses one of the antennas of the Mullard Radio Astronomy Observatory (MURA). MURA is comprised of several radio telescopes with antennas of different sizes and for the sake of comparison, it is assumed that the antenna has a radius of 25 m. The gain values of the antennas are shown in Table 1. Knowing the radius of the antenna and assuming an efficiency of 70%, the antenna gain can be computed using [27]:

$$G = e_A \left(\frac{\pi d}{\lambda} \right)^2 \tag{13}$$

where e_A is the antenna efficiency, d is the antenna diameter and λ the operating wavelength.

As discussed in Section 2, the transmitted waveform is a LFM chirp. The rest of the parameters for the simulation are presented in Table 2 as per refs. [28, 29].

It should be mentioned that circular polarisation is chosen as it minimises the amount of power loss due to the Faraday effect in the L-band due to the ionosphere [30]. Furthermore, the various issues that the ionosphere introduces, such as phase errors or frequency shifting, should be solved. In ref. [31] a method based on the *map drift* algorithm was proposed to correct the ionospheric anomalies in the case of spaceborne without the knowledge of electron content level. This gives a great advantage of other methods that heavily rely on that knowledge, such as in ref. [32], where the conducted study demonstrated that a dawn-dusk sun-synchronous orbit minimised the artefacts in the received signal, which could be removed by using a background ionosphere model. Certainly, this methods work for radar signals sent from the space to the Earth. However, similar methods could be applied to the case studied in this paper.

3.2 | Targets

In order to test the feasibility of the system, targets at different altitudes will be simulated. For the LEO case, a synthetic orbit will be simulated at different altitudes. For the geostationary case, the orbit of the Alcomsat 1 satellite will be replicated. The precise values of the orbit parameters are shown in Table 3. The parameters for the Alcomsat 1 have been extracted from the TLEs from the 16th of January 2020. TLEs are files that contain orbital elements, thanks to which the position of a target can be computed and propagated [14].

The size of the Alcomsat satellite is $2.36 \times 2.1 \times 3.6$ m^3, while the size of the LEO satellite will be around half the size

TABLE 1 Gain values for MHR and MURA.

	Gain
MHR	55.29 dB
MURA	55.0 dB

TABLE 2 Transmitter parameters.

Centre frequency (f_{op})	1.295 GHz
Bandwidth (B_W)	2 MHz
Peak power	3000 kW
Pulse width (T_p)	1 ms
Pulse repetition interval (PRI)	25 ms
Pulse repetition frequency (PRF)	40 Hz
Max. Average power	120 kW

of a Starlink satellite, that is $75 \times 30 \times 20$ cm^3, not taking into account the size of the solar panels.

The monostatic RCS chosen for the link budget has been determined using a physical optics (PO) method [33, 34]. The RCS was computed using the PO method along all azimuths and elevations of the supposed cuboids, after which the mean was computed. Then 3 dB were subtracted from the mean and the obtained value was used to calculate the link budget in Section 3.3.

3.3 | Link budget and visibility analysis

This section evaluates the possible observation time and the expected SNR of the proposed system for the different chosen targets. During this procedure, the parameters from Section 3.1 are going to be used.

Regarding the visibility time of the targets, the observation time of the GEO target is virtually infinite since the position of the GEO satellite does not practically change. To compute the visibility of the LEO target, the orbits have been propagated for 24 h and it has been assumed that the radio telescopes are able to see the target, that is, the beams of the transmitting and receiving antennas hit the target, as long as the elevation is greater than 8.1°. This minimum elevation angle is chosen after the minimum elevation angle used during observations on the Effelsberg Radio Telescope [35].

Figure 2 shows the target visibility time for the afore-mentioned 24 h. As one could expect, the observation time increases as the altitude is higher. If the target is at a lower height, it might occur that it can hide under the perceived horizon of either the transmitter or the receiver, resulting in smaller visibility times. Specifically, for a target orbiting at 1100 km the observation time is 30 s which might not be enough to ensure detection. In the case of an altitude of 1200 km the visibility time of the target would be 2.5 min that should be enough to ensure detection. At higher altitudes the observation time of the possible targets increases, reaching a maximum of around 30 min at 2200 km.

The SNR is computed using the RRE in for a bistatic configuration assuming coherent integration [7] during the periods where the target is visible:

$$\text{SNR}_{\text{bs}} = n_p \frac{P_t G_t G_r G_{sp} \lambda^2 \ \text{RCS}_{\text{bs}}}{(4\pi)^3 R_1^2 R_2^2 k T_0 F B_W L_s} \tag{14}$$

TABLE 3 Orbit parameters and RCS for targets.

	Alcomsat 1	LEO target
Norad ID	43,039	-
Inclination (°)	12×10^{-3}	52
Eccentricity	2.16×10^{-4}	2.54×10^{-4}
Altitude (km)	35 794.72	[1200 − 2200]
RCS	15.17 dB m^{-2}	−17.61 dB m^{-2}

where

- n_p is the number of coherently integrated pulses. For the simulations $n_p = 25$ for the LEO target and $n_p = 50$ for the GEO target.
- P_t is the transmitting power
- G_t is the transmitter antenna gain
- G_r is the receiver antenna gain
- G_{sp} is the signal processing gain, defined as

$$G_{sp} = T_p \cdot B_W \qquad (15)$$

- λ is the operating wavelength
- R_1 is the distance from the transmitter to the target
- R_2 is the distance from the target to the receiver
- k is the Boltzmann constant
- T_0 is the reference noise temperature, 290 K
- F is the noise factor. In this case, $F = 3.62$ dB, derived from the 150 K system temperature from the technical notes of the MHR [36].
- The losses, L_s, comprise four different categories:
  - System losses, which are 6 dB, accounting for 3 dB per path.
  - Dry air atmospheric losses. Which for a two-way path are estimated at 2.4 dB.
  - Atmospheric losses for air containing vapour water, to account for any cloud or humid environment assumed at 2.6 dB.
  - Tropospheric losses, assumed at 1.6 dB.

The mean SNR for the geostationary target is 19.60 dB with a variation of $\pm 5.72 \times 10^{-6}$ dB. As the relative position of the Alcomsat satellite does not change much, the resulting SNR has little variation during the observation time. On the contrary, the SNR for the LEO target, Figure 3, varies noticeably, specially as the altitude increases. It can be observed that, because of the visibility time, the SNR variation increases as the altitude is higher. Additionally, as the altitude heightens the mean of the SNR decreases (Figure 3).
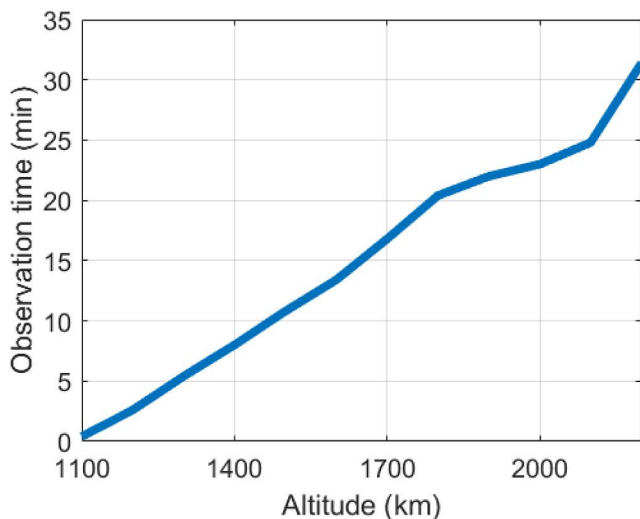
4 | SYSTEM PERFORMANCE

Having assessed the feasibility of the radar system, this section investigates the performance of the proposed long baseline radar under different sensor and target configurations. For measuring the ambiguity of the radar measurements the multiple-input-multiple-output (MIMO) ambiguity function (AF), introduced in Section 2.3 will be used.

4.1 | Simulated scenarios

The different radar configurations examined in this analysis are summarised as follows:

- Monostatic case. In the case of the monostatic configuration, the transceiver will be placed in the same location as the MHR antenna.
- Bistatic case. In the case of the bistatic case, the receiver will be placed depending on which multistatic receiver configuration is being studied. The different receiver configuration cases are presented in the next point.
- Multistatic case. In the multistatic case, only one transmitter is assumed, located in MHR, while several receiver configurations are considered:

Case 1. Cluster of receivers. The main advantage of the cluster, or any of the multiple receiver configurations, is that the overall SNR would increase by the number of receivers. Also, it would be easier to synchronise and manage the receivers if they are closer.

Case 2. Receivers spread throughout the world. The spread configuration would allow to decrease the ambiguity as the target is observed between different angles. However, separating the receivers so far from each other, would make synchronisation challenging.
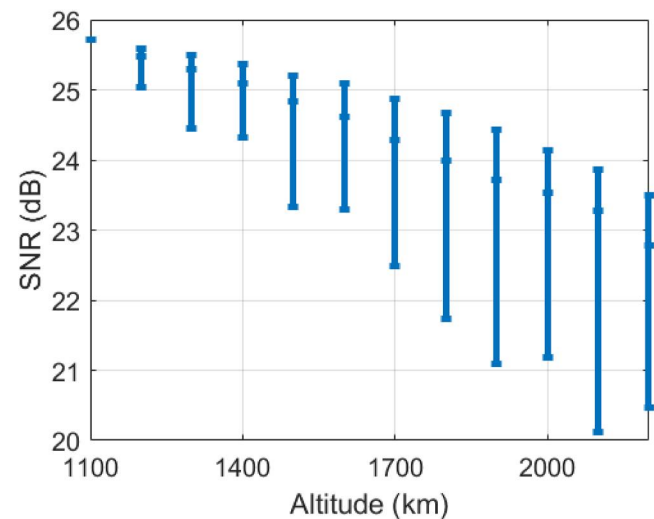

FIGURE 2 Target visibility time.

FIGURE 3 SNR variation for 24 h for LEO target.

Case 3. Combination of both Case 1 and Case 2.

The different positions of the receivers are shown in Figure 4. A more detailed explanation of the different receiver configurations, as well as their precise location of all of them, is presented in Appendix A.1.

4.1.1 | Receiver and transmitter parameters

By virtue of simplicity, an SNR of 22 and 19.60 dB is assumed for the LEO and GEO targets, respectively, at the receiver after the matched filter and multiple integration. The SNR after the matched filter and the multiple coherent integration can be calculated as follows:

$$SNR = SNR_{ant} + 10\log(n_{Pulses}) + 10\log(G_{sp}) - 3\,\mathrm{dB}$$
$$= SNR_{ant} + 10\log(n_{Pulses}) + 10\log(T_p \cdot B_W) - 3\,\mathrm{dB} \quad (16)$$

where the extra 3 dB are to account for estimation or processing errors. So, using parameters from Table 2, for achieving $SNR_{LEO} = 22$ dB and $SNR_{GEO} = 19.60$ dB, the SNR before the antenna should be $SNR_{ant,LEO} = -18.01$ dB and $SNR_{ant,GEO} = -23.30$ dB, respectively.

4.1.2 | Targets

Two targets at different altitudes will be simulated for the examined scenarios: one target at LEO and another target at GEO, at altitudes of 1200 km and 35,795 km, respectively. Since it is assumed that the SNR is fixed, the targets are not considered to have a particular size or RCS.
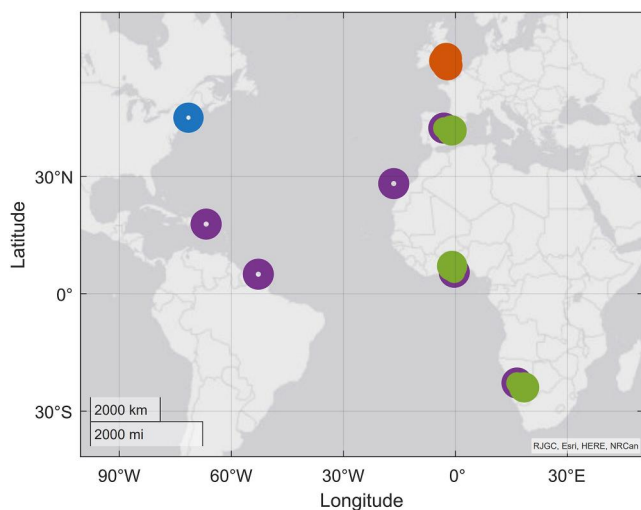

FIGURE 4   Position of the transmitter (blue) and receivers (orange for Case 1, purple for Case 2 and green for Case 3).

4.2 | Results and discussion

For computing the MIMO AF, two scenarios are considered. On the first instance, it is assumed that there is no Doppler processing, thus no speed estimates. In the second scenario, Doppler processing will be implemented.

As discussed, two satellites are going to be simulated at altitudes 1200 km and 35,795 km. The MIMO AF will be computed for the monostatic case, for one of the bistatic pairs, (9), and for the coherent and non-coherent multistatic cases. Notice that the (0, 0, 0) in the MIMO AF represents the position of the target. Furthermore, the graphs will show the (x, y) cut of the $z = 0$ m plane.

4.2.1 | MIMO AF with speed estimates

For this set of results, the MIMO AF is computed using Equation (10) for the non-coherent fusion and Equation (11) for the coherent fusion. Some of the results that are going to be displayed present some errors in the Doppler estimation. Nonetheless, because of the multiple fusion the final MIMO AF still presents the target in the correct position. It is worth mentioning that only the results of the (x, y) cut of the LEO target are shown, since the results of the GEO target are very similar to the results observed when no Doppler processing was done.

In the following figures, the red lines represent the -3 dB limits. The -3 dB lines will define the uncertainty or ambiguity in the measurement. The -3 dB levels will give a measure on the possible location and the resolution of the system and not a detection threshold. Moreover, the detection performance will also depend on the chosen detector.

Case 1: cluster of receivers
Figure 5 shows the (x, y) cut for the $z = 0$ plane of the MIMO AF for the GEO case. First, it must be noted that the ridge in all the graphs is similar because the bistatic range also similar due to the configuration of the receivers. It can be noticed that the introduction of multiple readings from different receivers reduces the uncertainty for the multistatic cases, whether it is coherent or non-coherent. The multistatic case for the non-coherent fusion, Figure 5b, shows that the main lobe has absorbed the sidelobes. The AF in the coherent case, Figure 5c, presents lower floor levels, the surroundings around the -3 dB levels are darker, and also lower uncertainty.

In Figure 6, the MIMO AFs after applying Doppler processing are shown. The first feature to notice is the decrease in ambiguity. Specifically, compared to the GEO target, the ridge has been replaced by a main lobe, Figure 6a. The non-coherent fusion, Figure 6b, has a similar same shape as the bistatic case, while the coherent fusion, Figure 6c, shows how the ambiguity has been highly reduced. One last thing to notice is that some of the bistatic pairs have had their Doppler estimated incorrectly, which derived in an artefact in the non-coherent fusion cut, Figure 6b. The main error that can be observed is the false location of the -3 dB levels, which seem to be off by a few hundred metres.
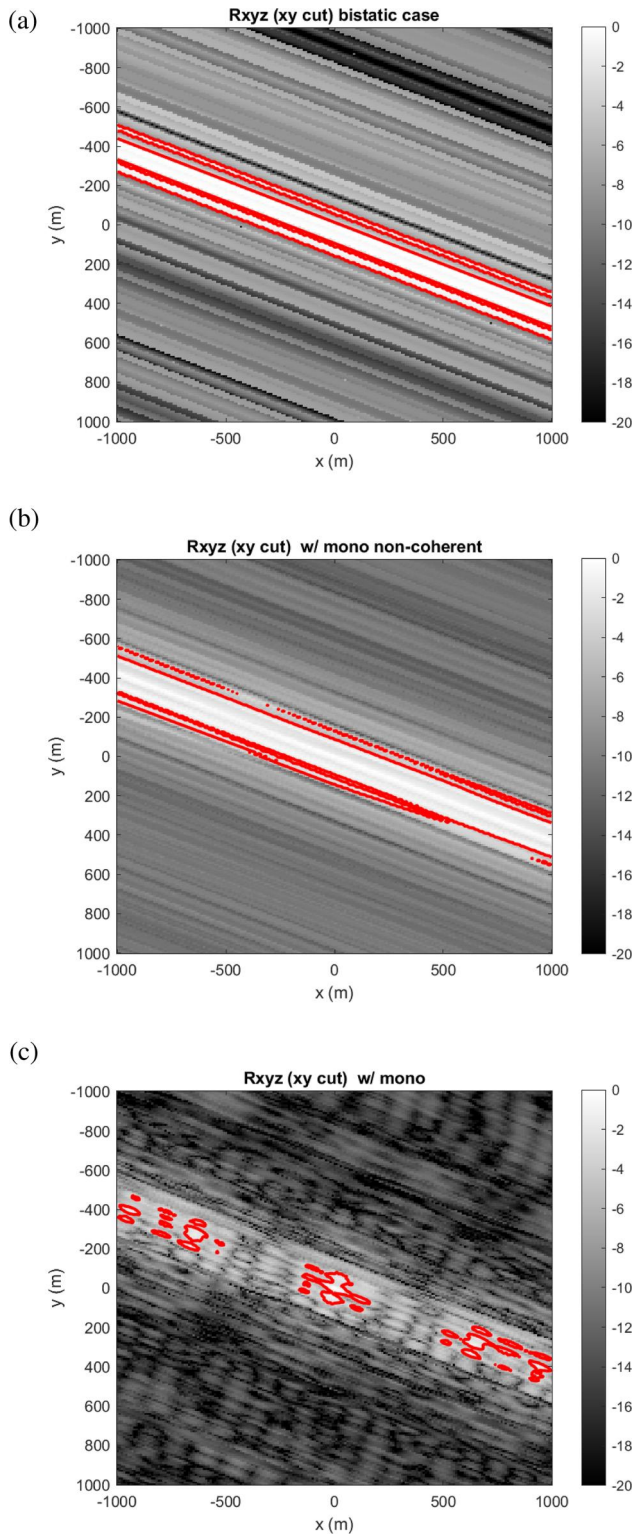
(a)

(b)

(c)

FIGURE 5 Case 1, (x,y) cut, alt. = 35 795 km. (a) Bistatic case. (b) Non-coherent fusion. (c) Coherent fusion.

(a)

(b)

(c)

FIGURE 6 Case 1, (x,y) cut, alt. = 1200 km. (a) Bistatic case. (b) Non-coherent fusion. (c) Coherent fusion.

Case 2: receivers spread throughout the world

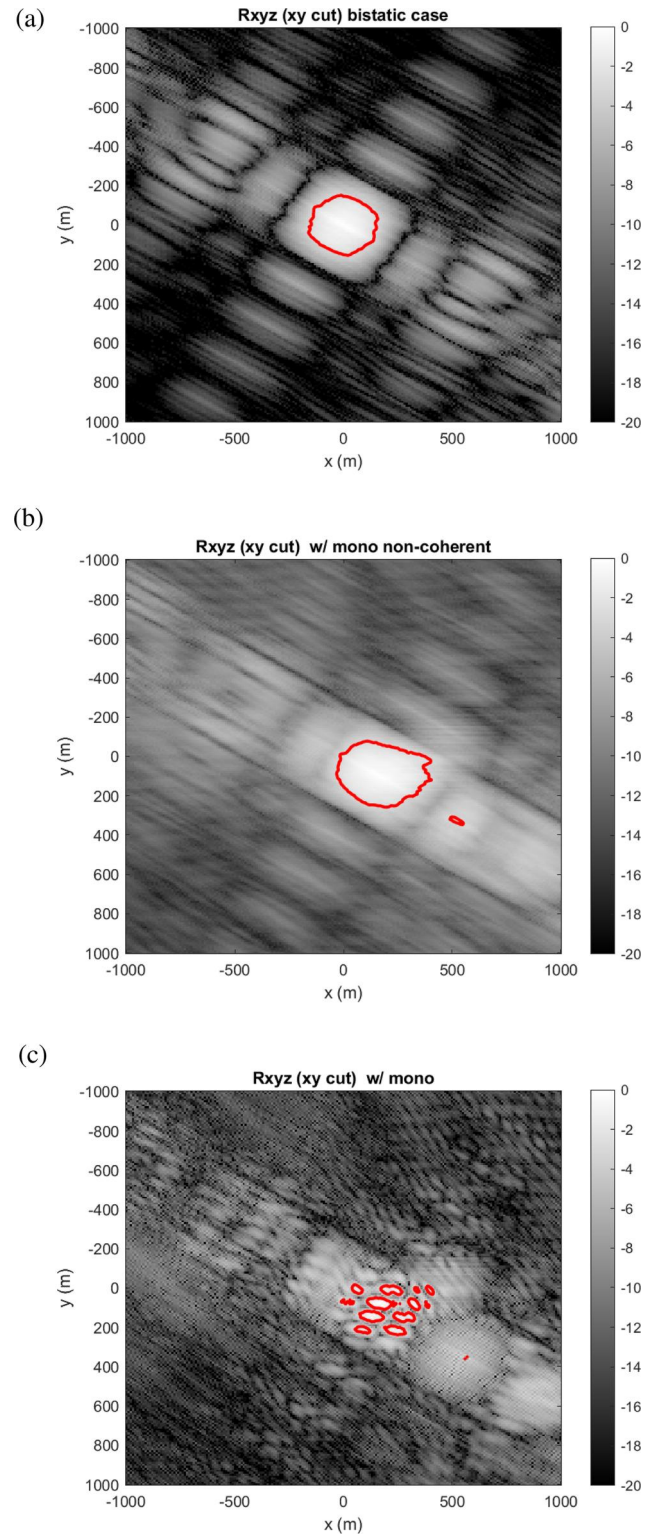Similarly, as in Case 1, the bistatic AF for a GEO altitude target, see Figure 7a, presents a ridge. This is due to the GEO altitude diminishing the effect of the bistatic configuration, as the bistatic angle, around 8°, is small. However, as each MIMO AF is different for each bistatic pair, when fusion is applied, see Figures 7b and 7c, the ambiguity in the final MIMO AF is reduced. For the coherent fusion, Figure 7c, although it seems

not to show major peaks are present, a maximum peak is present in (0, 0). The ambiguity for these case has been reduced when compared to the previous scenario, Figure 5c.

For the LEO case, the Doppler in the presented bistatic case, Figure 8a, has been incorrectly estimated. This has resulted in the maximum changing position and the target perceived on another location. However, due to the monostatic and the rest of the bistatic readings, the maximum of the multiple fusion occurs in the correct position of the target, Figures 8b and 8c. At the same time, because of this error, and
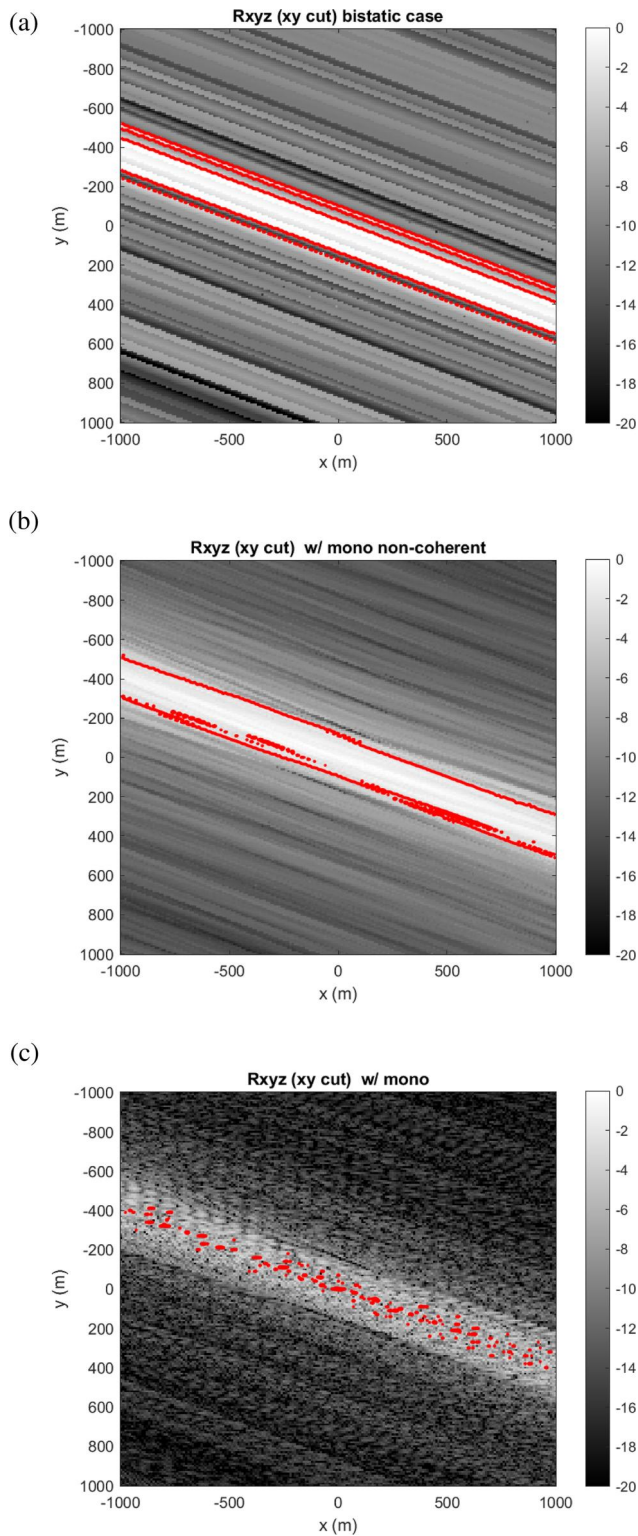
FIGURE 7 Case 2, (x,y) cut, alt. = 35,795 km. (a) Bistatic case. (b) Non-coherent fusion. (c) Coherent fusion.
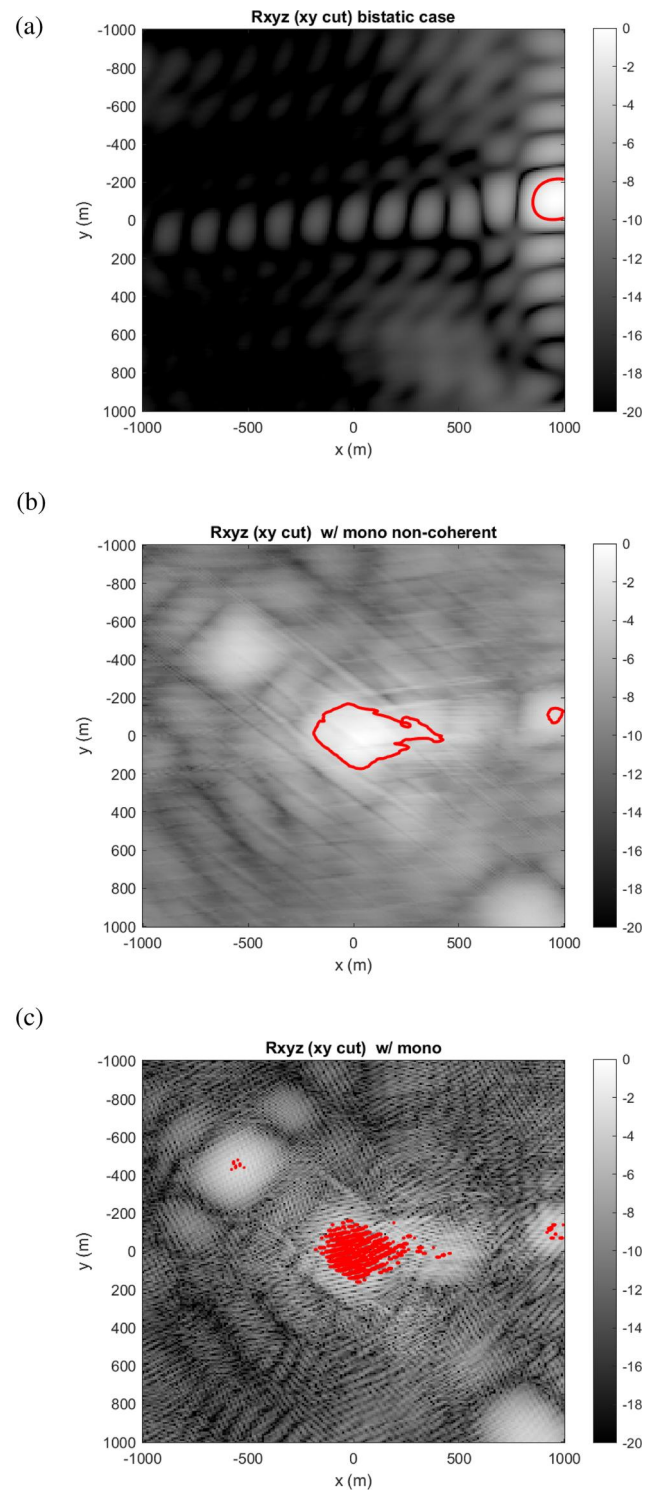

FIGURE 8 Case 2, (x,y) cut, alt. = 1200 km. (a) Bistatic case. (b) Non-coherent fusion. (c) Coherent fusion.

some other miscalculations in the other bistatic AFs in the case of the coherent fusion, there are some artefacts that might led to a wrong estimation of the location. The coherent fusion, Figure 8c, presents smaller ambiguity than the non-coherent case, Figure 8b. However, compared to Case 1, the ambiguity seems to be more spread along smaller lobes, instead of several thicker lobes, Figure 6c.

Case 3: clusters spread throughout the world

For the third and final case, the multistatic AF of the coherent case, Figure 9b, presents lower ambiguity than the ridge shaped AF of the non-coherent case, Figure 9a. No major improvements have been observed from Case 2.

Case 3 does not present any significant changes from the previous cases for the LEO target. The multiple fusion graphs, Figures 10a and 10b, show almost identical outcomes as in Cases 1 and 2 for the non-coherent fusion. In the case of the coherent fusion, as in Case 2, the ambiguity is spread throughout multiple main lobes, although these seem to be less, and more concentrated around the true position of the target.
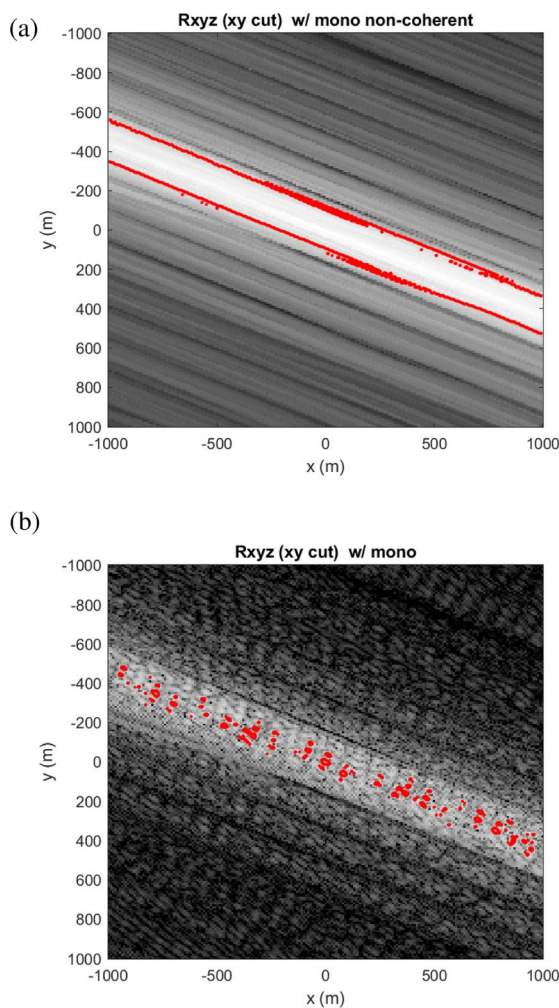
5 | CONCLUSIONS AND FUTURE WORK

In this paper, a long baseline multistatic radar system was proposed as a potential solution for SSA. The results from the feasibility analysis have proven that the SNR would be enough for the detection of certain targets. Furthermore, the results of MIMO AF analysis for the multistatic system shows that the extension from bistatic to multistatic gives advantages in localisation performance and reduction in the ambiguity measurement. Using the MIMO AF, the system was assessed under different target-receivers configurations. Results demonstrated that distributed scenarios generally outperform co-located receivers; however, accounting for synchronisation challenges in remote receivers, clusters of receivers operating coherently can be a good alternative. While coherent fusing performs significantly better than non-coherent in all scenarios, proper synchronisation between all the sensors can be very challenging, especially in highly distributed geometries.

Moreover, comparing the results for different target-sensor configurations demonstrated that distributed systems have an
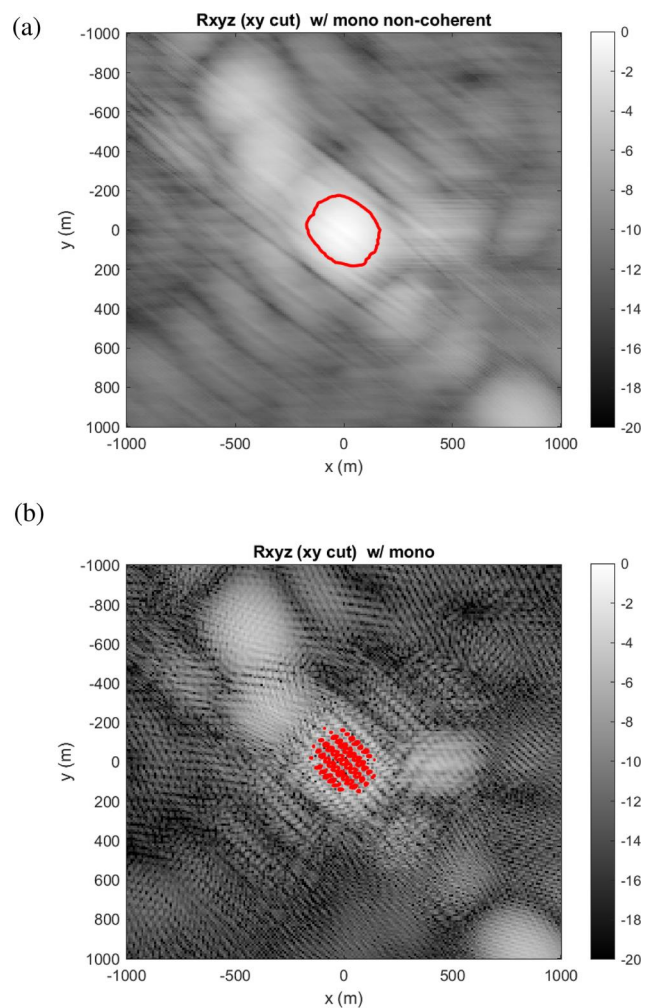

FIGURE 9 Case 3, (x,y) cut, alt. = 35,795 km. (a) Non-coherent fusion. (b) Coherent fusion.

FIGURE 10 Case 3, (x,y) cut, alt. = 1200 km. (a) Non-coherent fusion. (b) Coherent fusion.

advantage over swarms of receivers. This becomes more apparent for targets in lower altitudes where the bistatic angle increases even more. The target is observed from different sides, which results in different bistatic AFs and, when combined, produces an AF with less ambiguity. Nevertheless, in terms of system implementation, it should be noted that having access to several receivers in different countries and continents can be very challenging. Hence, the cluster of receivers (Case 1) might be more applicable. Furthermore, as the altitude of the target increases, see GEO, the advantages of spread receivers start to diminish and therefore a clustered configuration where coherence fusion could be achieved would be more desirable. It must be noted that the results in Case 3 were more accurate and presented less ambiguity than the previous two cases. The reason is that compared to Case 1, since all the receivers are in the same location, many of them will present similar processing errors, and compared to Case 2, having less receivers spread through the world will lead to less possible errors. As a consequence, Case 3 is the optimal case.

Future work will involve the development of the Doppler compensation techniques in the case where the perceived Doppler shift in the receivers is different from each other. Related to the speed of the target and the resulting Doppler shift is the processing needed to overcome the aliasing in LEO targets. Certainly, another point to be tackled is the correct estimation of the Doppler when multiple targets are present.

AUTHOR CONTRIBUTION

ACKNOWLEDGEMENTS

CONFLICT OF INTEREST STATEMENT

None.

DATA AVAILABILITY STATEMENT

The data that support the findings of this study are available from the corresponding author upon reasonable request.

ORCID

Sebastián Díaz Riofrío 🅭 https://orcid.org/0000-0002-0640-0385
Carmine Clemente 🅭 https://orcid.org/0000-0002-6665-693X

REFERENCES

1. Esa's Annual Space Environment Report," Tech. Rep., ESA Space Debris Office, (2022)
2. Marchetti, E., et al.: Space-based sub-thz isar for space situational awareness - laboratory validation. IEEE Trans. Aero. Electron. Syst. 58(5), 4409–4422 (2022). https://doi.org/10.1109/taes.2022.3160985
3. Persico, A.R., et al.: Cubesat-based passive bistatic radar for space situational awareness: a feasibility study. IEEE Trans. Aero. Electron. Syst. 55(1), 476–485 (2019). https://doi.org/10.1109/taes.2018.2848340
4. Saillant, S.: Bistatic space-debris surveillance radar. In: 2016 IEEE Radar Conference (RadarConf), pp. 1–4 (2016)
5. Technical Report on Space Debris," tech. rep., (1999)
6. Scanning, observing. https://www.esa.int/Space_Safety/Space_Debris/Scanning_and_observing2
7. Richards, M.A. (ed.) Principles of Modern Radar: Basic Principles. Radar, Sonar and Navigation. Institution of Engineering and Technology (2010)
8. Reising, C., et al.: Gestra - upgrading to future distributed phased array radar networks for space surveillance. In: 2022 IEEE International Symposium on Phased Array Systems and Technology (PAST), pp. 1–8 (2022)
9. Bordoni, F., et al.: Saocom-cs sar imaging performance evaluation in large baseline bistatic configuration. In: 2015 IEEE International Geoscience and Remote Sensing Symposium (IGARSS), pp. 2107–2110 (2015)
10. Welch, S., et al.: Long baseline radar bistatic measurements of geostationary satellites. In: 2022 19th European Radar Conference (EuRAD), pp. 1–4 (2022)
11. da Graça Marto, S., et al.: Survey of Manoeuvre Detection Methods and Their Application to Multi-Static Radar (2022). AMOS 2022 ; Conference date: 27-09-2022 Through 30-09-2022
12. Píriz, R., et al.: A cost-efficient regional synchronization system. In: 2017 Joint Conference of the European Frequency and Time Forum and IEEE International Frequency Control Symposium, pp. 683–685. EFTF/IFC (2017)
13. Filho, E.R.S., Cassola, M.R.: Experimental evaluation of gnss-based frequency synchronization for sar applications. In: IGARSS 2022 - 2022 IEEE International Geoscience and Remote Sensing Symposium, pp. 7164–7167 (2022)
14. Basic Description of the Two Line Element (Tle) Format." https://www.space-track.org/documentation#/tle
15. De Maio, A., Greco, M.: Modern Radar Detection Theory. Electromagnetics and Radar. Institution of Engineering and Technology (2015)
16. Laghezza, F., et al.: Italian bistatic radar system for surveillance of space debris in low earth orbit. In: 2010 IEEE Radar Conference, pp. 220–224 (2010)
17. Kell, R.: On the derivation of bistatic rcs from monostatic measurements. Proc. IEEE 53(8), 983–988 (1965). https://doi.org/10.1109/proc.1965.4077
18. Chen, V.: The Micro-doppler Effect in Radar, ed (2019)
19. Ilioudis, C., Clemente, C., Soraghan, J.: Gnss-based passive uav monitoring: a feasibility study. IET Radar, Sonar Navig. 14(4), 516–524 (2020). https://doi.org/10.1049/iet-rsn.2019.0308
20. Papoutsis, I., Baker, C., Griffiths, H.: Netted radar and the ambiguity function. In: IEEE International Radar Conference, 2005, pp. 883–888 (2005)
21. Derham, T., et al.: Ambiguity functions for spatially coherent and incoherent multistatic radar. IEEE Trans. Aero. Electron. Syst. 46(1), 230–245 (2010). https://doi.org/10.1109/taes.2010.5417159
22. Capó-Lugo, P.A., Bainum, P.M: 2 - two body orbital motion. In: Orbital Mechanics and Formation Flying .A. Capó-Lugo and P.M. Bainum, (Eds.), pp. 7–35, Woodhead Publishing. (2011)
23. Zhang, Q., et al.: Near-space topsar large-scene full-aperture imaging scheme based on two-step processing. Sensors 16(8), 1177 (2016). https://doi.org/10.3390/s16081177
24. Sy, O.O., et al.: Simulation of earthcare spaceborne Doppler radar products using ground-based and airborne data: effects of aliasing and nonuniform beam-filling. IEEE Trans. Geosci. Rem. Sens. 52(2), 1463–1479 (2014). https://doi.org/10.1109/tgrs.2013.2251639

25. Zhan, M., et al.: Coherent accumulation detection for a maneuvering target with Doppler ambiguity and Doppler aliasing. In: IET International Radar Conference, vol. 2020, pp. 1421–1424. IET IRC 2020) (2020)

26. Peterson, K.M.: Satellite communications. In: Encyclopedia of Physical Science and Technology. R.A. Meyers, (Ed.), (pp. 413–438) New York: Academic Press. (2003)

27. MINOLINO: SATELLITE SYSTEMS ENGINEERING IN AN IPV6 ENVIRONMENT, 1 ed. CRC PRESS (2009)

28. "Space surveillance sensors: The millstone hill radar (may 5, 2012)." https://mostlymissiledefense.com/2012/05/05/space-surveillance-sensors-%20millstone-hill-radar/

29. Buonsanto, M.: Millstone Hill," Tech. Rep. MIT Haystack Observatory (1992)

30. Iida, T., Wakana, H.: Communications satellite systems. In: Encyclopedia of Physical Science and Technology (ed) R.A. Meyers (Ed.), pp. 375–408, New York: Academic Press. (2003)

31. Nandy, P.S., Putrevu, D.: Impact of ionosphere on high-bandwidth chirp in L-band SAR and its mitigation. In Earth Observing Missions and Sensors: Development, Implementation, and Characterization IV. J. Xiong, S.A. Kuriakose, T. Kimura (Eds.), (Vol. 9881, p. 98811Q). International Society for Optics and Photonics. (2016)

32. Chapin, E., et al.: Impact of the ionosphere on an l-band space based radar. In: 2006 IEEE Conference on Radar (2006).8

33. Jakobus, U., Landstorfer, F.: Improved po-mm hybrid formulation for scattering from three-dimensional perfectly conducting bodies of arbitrary shape. IEEE Trans. Antenn. Propag. 43(2), 162–169 (1995). https://doi.org/10.1109/8.366378

34. Rcs - Matlab." https://uk.mathworks.com/help/antenna/ref/rcs.html

35. Technical Characteristics of the Effelsberg 100-m Radio Telescope."http://www.mpifr-bonn.mpg.de%20/div/effelsberg/antenna/antenna_spec.html

36. Laboratory, L.: The Millstone Hill Propagation Study: Progress in Fy 1970 (1970)

APPENDIX A

Receivers positions

Case 1: Cluster of receivers. The cluster of receivers takes its location from the eMerlin radio telescope network based in the UK. The chosen locations are:

- Jodrell Bank:
  * Lovell telescope. Coordinates (53.2366, −2.3085, 10)
  * Mark II telescope. Coordinates (53.2339, −2.3039, 10)
- Pickmere. Coordinates (53.2886, −2.4453, 10)
- Darnhall. Coordinates (53.1563, −2.5357, 10)
- Knockin. Coordinates (52.7902, −2.9971, 10)
- Defford. Coordinates (52.1005, −2.1443, 10)

Case 2. Receivers spread throughout the world. The positions of these receivers are based on pre-existing radio telescopes or observatories. Evidently, many of these pre-existing radio telescopes function at a different operating frequency than the one used in MHR, but it is assumed in the simulation that every receiver works at the same frequency.

The locations of the receivers are:

- Namibia. There is a radio telescope in Namibia part of the High Energy Stereoscopic System (H. E.S.S.). Coordinates (−23.2713, 16.5001 1800)
- Spain. This receiver is located in the Yebes Observatory. Coordinates (40.5241, −3.0893, 980)
- Canary Islands. The receiver would be based in the Teide Astronomic Observatory. Coordinates (28.2986, −16.5106, 2400)
- Ghana. The receiver in Ghana is located in the Ghana Radio Astronomy Observatory. Coordinates (5.7503, −0.3051, 70)
- Guyana. Although there is no radio telescope, it is assumed that the receiver would be located in the rocket launch facilities of the French Guyana. Coordinates (5.2264, −52.7774, 2)
- Puerto Rico. The antenna would be located in the old Arecibo Observatory. Coordinates (18.3442, −66.7526, 498)

Case 3. Combination of both Case 1 and Case 2. For this case there would be two receivers per cluster. The distance between the receivers in the cluster is around 200 km. The locations of the receivers are:

- Namibia. One of the receivers will be placed in the H.E.S.S. and the other one will be placed 200 km from there. The coordinates are:
  * Namibia I: (−23.2713, 16.5001, 1800)
  * Namibia II: (−24.3455, 18.4017, 1177)
- Ghana. The first receiver will be placed in the same place as in the previous configuration, the Ghana Radio Astronomy Observatory, the second one 200 km away from there. The coordinates are:
  * Ghana I: (5.7503, −0.3051, 70)
  * Ghana II: (7.4244, −0.8833, 70)
- Spain. One of the receivers will be placed on the Yebes Observatory and the other one will be placed on the Javalambre Astrophysics Observatory. The coordinates of the receivers would be:
  * Spain I: (40.5241, −3.0893, 980)
  * Spain II: (40.0419, −1.0162, 1957)